2021

Energy Release and Fragmentation of Brittle Aluminum Reactive Material Cases

Kline, Jacob C.; Mason, Brian P.; Hooper, Joseph P.

Wiley

Kline, Jacob C., Brian P. Mason, and Joseph P. Hooper. "Energy Release and Fragmentation of Brittle Aluminum Reactive Material Cases." Propellants, Explosives, Pyrotechnics (2021).
http://hdl.handle.net/10945/67438

Full Paper

Propellants, Explosives, Pyrotechnics

DOI: 10.1002/prep.202100014

Energy Release and Fragmentation of Brittle Aluminum Reactive Material Cases

Jacob C. Kline,[a] Brian P. Mason,[a] and Joseph P. Hooper*[a]

Abstract: Cylindrical reactive material cases produced by the consolidation of an aluminum powder were tested via explosive launch in a closed chamber. One configuration measured the quasistatic overpressure generated by the case and explosive, and two further tests focused on soft-catch of fragments before and after striking the chamber walls. On a volumetric basis, the reactive material cases produced two to three times the combustion energy of an aluminum 6061 alloy case or a bare nitromethane explosive that was tested as comparisons. The metal combustion primarily occurs after case fragments impact the walls. Increasing the reactive material case thickness produces a higher pressure but lower combustion efficiency per unit mass, despite producing comparable or slightly more fine fragments on a per gram basis. Though the brittle, pressed aluminum cases have low toughness and tensile strength, recovered fragment patterns show a range of fragment sizes up to 1 mm, with approximately one-third of the mass below 100 μm.

Keywords: Reactive Materials · Energetic Materials · Fragmentation

1 Introduction

In this work, the fragment distributions of aluminum reactive material (RM) cases made from pressed powder are presented, along with the quasistatic overpressures they generate inside a closed volume. Reactive materials such as the one considered here are designed to fracture heavily upon explosive launch or impact with a target. The resulting debris combusts and can generate overpressure and produce incendiary effects within confined spaces. Aluminum powders have long been studied as a primary ingredient for reactive materials due to their high enthalpies of combustion [1–6], and are frequently combined with other metal powders to alter the mechanical or chemical properties. Several authors have also explored mixing or milling the powders with polymer binders, such as PTFE [7–10].

Less work has been done to examine the fragment distributions of reactive materials, which are challenging to study due to the large quantity of extremely fine debris produced and the difficulty of recovering it while suppressing combustion and further breakup [11–13]. The size distribution of fragments is particularly important for aluminum, whose ignition temperature is dependent on the particle size and external heating rate [14,15]. Trunov et al. reviewed ignition temperatures of aluminum particles at ambient pressure and showed that they span a wide range in the literature. Ignition of particles larger than 75–100 μm required temperatures approaching the alumina melting point (2053 °C), while finer particles were considerably lower (600–800 °C) [15]. Thus the generation of fine fragments from a reactive material is closely linked to the combustion energy it releases. In this work, a prototypical aluminum reactive material made from isostatically compacted powder is formed into naturally fragmenting cases. Explosive tests in a closed chamber are then used to study their energy release and fragmentation. A combination of soft-catch media and inert atmosphere tests are used to analyze the separate fragmentation processes occurring on explosive launch and after impact with the chamber walls.

2 Experimental Section

2.1 Methodology

Spherical aluminum powder of nominal average particle size 16 μm was procured from Valimet Inc. (Stockton, CA, USA), under the trade name H15. This powder was consolidated via cold isostatic pressing (CIP) into cylindrical cases of 2.54 cm inner diameter using a wet bag technique with polyurethane molds and a steel mandrel insert. After pressing, the cases were heat-treated at 200 °C for 30 minutes to remove residual stresses from the pressing process. Previous work on similar aluminum compacts [16,17]

[a] J. C. Kline, B. P. Mason, J. P. Hooper
Department of Physics
Naval Postgraduate School
1 University Circle, Monterey, CA
Phone: 1 +(831) 656-2385
*e-mail: jphooper@nps.edu

Supporting information for this article is available on the WWW under https://doi.org/10.1002/prep.202100014

demonstrated that this mild heat treatment does not result in sintering or oxidation. Following heat treatment, the cases were machined to achieve uniform outer diameters of approximately 3.4 and 3.9 cm, with an overall length of 7.62 cm. These dimensions result in reactive material case mass to high explosive charge mass ratios (M/C ratios) of approximately 2 and 3 with respect to the sensitized nitromethane explosive used here. A photograph of the machined cases is shown in Figure 1a, and the final charge assembly with RM case, end caps, and the detonator is shown in Figure 1b.

Mechanical properties of the pressed Al material were tested with solid right cylinders of 10 mm diameter and lengths of 5 or 10 mm. Dynamic measurements were taken with a split Hopkinson pressure bar (SHPB) system utilizing a momentum trap and 19.05 mm diameter C350 maraging steel bars. All Hopkinson bar tests were performed with a copper pulse shaper of 0.53 mm thickness with the bar/sample interface lightly greased to minimize friction.

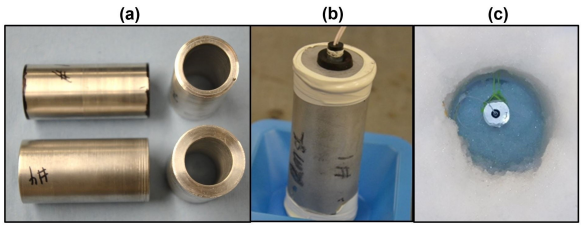

Figure 1. Aluminum RM cases: **(a)** Pressed H15 Al cases with M/C ratios of 2 (top) and 3 (bottom) **(b)** Charge assembly with pressed RM case, HE fill, and detonator **(c)** Charge assembly in snow soft-catch cavity.

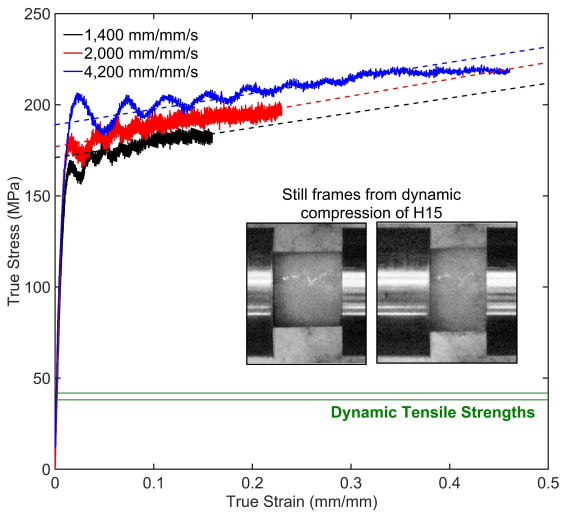

Figure 2. SHPB testing of pressed aluminum samples. Linear fits of the plastic strain region are given as dashed lines.

2.2 Material Properties

Stress-strain curves of the pressed aluminum RM from Hopkinson bar testing are presented in Figure 2, showing dynamic compressive strengths that range from ~165 MPa to 200 MPa, roughly linear work hardening, and a mild strain-rate dependence. These values for compressive strength are distinctly lower than those for a similar compact made with a smaller particle size (~3.5 μm, trade name H2) pure aluminum discussed in previous work [16, 17]. Considerable compressive plastic strains can be applied to the samples without macroscopic failure. Longitudinal and shear sound speeds were calculated using a pulse-echo technique with an ultrasonic probe and corresponding couplant. The calculated effective elastic and shear moduli from the wave speeds are significantly less than those of bulk aluminum. The K_{Ic} fracture toughness was determined using notched 3-point bend samples machined to ASTM E399 specifications by electrical discharge machining. Material properties of the reactive aluminum case are shown in Table 1, along with the corresponding values of bulk aluminum 6061-T6 which is used as a baseline in explosive tests.

Due to the brittleness of these metal compacts (comparable in toughness to a ceramic), a Brazilian type test, commonly used in the study of brittle geomaterials [18–20] provided information on the dynamic tensile properties of these samples. The dynamic tensile strength calculated from Brazilian tests was approximately 40 MPa, considerably lower than the dynamic compressive strength of the compact. This compressive/tensile strength disparity is typical of many reactive materials [16, 17, 21, 22].

2.3 Detonation Procedure

All explosive testing in this work took place in a sealed cylindrical steel test chamber 1.91 cm thick. Its internal length and diameter were both 101.6 cm, giving an internal volume of 0.861 m^3 including instrumentation viewports. An image of the test chamber is shown in the inset of Figure 3.

Table 1. Mechanical properties.

	Reactive case (H15 Al)	Al 6061-T6
Mean case density (g/cm^3)	2.56 +/−0.08	2.70
Mean case porosity (%)	5.2	–
Quasistatic fracture toughness (MPa $m^{0.5}$)	3.1 +/−0.5	29
c_l (longitudinal sound speed, m/s)	4730	6320
c_s (shear sound speed, m/s)	2530	3130
Elastic modulus (GPa)	43.2	68.9
Shear modulus (GPa)	16.6	26.0
c_p (approx. plastic wave speed in uniaxial stress, m/s)	180	–

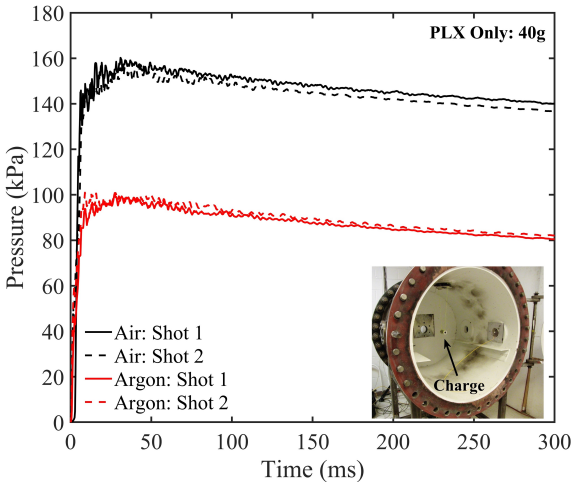

Figure 3. Overpressure versus time for bare HE charges with no reactive material cases. **Inset:** Test chamber with charge suspended in the center.

Shots were conducted for a bare high explosive charge as well for a high explosive surrounded by a reactive material case. The explosive used was Picatinny Liquid Explosive (PLX), which is 95 wt% nitromethane sensitized with 5 wt% ethylene diamine. Charges were hung in the center of the chamber, roughly 50 cm from the radial chamber wall. For tests with no reactive material case, 40 g of liquid PLX was confined in a thin borosilicate glass vial 2.2 mm thick. For cased shots, the PLX was poured into the case and the endcaps were sealed to prevent leakage. The average explosive mass within the cases was 40.5 ± 0.3 g of PLX. RP-80 exploding bridge wire detonators (80 mg PETN, 123 mg RDX) were used in all tests. The overpressure inside the chamber was measured as a function of time using piezoresistive pressure transducers (Endevco 8530b-200). The resulting pressure data were run through a low pass filter with a cutoff frequency of 50 Hz to remove the high-frequency noise and then smoothed with a moving average filter with a 2.5 ms sliding window. The overpressure curves for the bare PLX charges are presented in Figure 3.

3 Results and Discussion

3.1 Bare High Explosive

To obtain a baseline quasistatic overpressure for the bare explosive, 40 g PLX charges with no reactive material case were detonated in the test chamber in both an air and argon environment. For the latter, the chamber was purged with argon gas for approximately 15 minutes prior to detonation.

The resulting overpressure from these shots is shown in Figure 3; the peak quasistatic overpressure corresponds to the maximum observed pressure value prior to the slow decay inside the chamber. The chamber overpressure is converted into an energy release in the following way. The energy release is approximated using the peak quasistatic overpressure point; this assumes that combustion is complete after this peak pressure. Some limited validation of this assumption is discussed below. In this section, only the detonation and afterburn of the high explosive charge are considered. These are assumed to heat the air in the chamber and increase its pressure. It is helpful to incorporate the temperature dependence of the specific heat capacity of air for this conversion. A simple linear dependence was fit to the NIST-JANAF thermochemical tables [23] to yield

$$c_v\,(T) = A + bT \tag{1}$$

with fit values of $A = 678.25$ J/kg K and $b = 0.1813$ J/kg K^2. Figure 4a shows this fit for air at several different constant pressures; the linear assumption is acceptable up to an average chamber temperature of at least 2000 K for the overpressures considered here. The process is assumed to be isochoric, as the chamber was tightly sealed. The energy release E_R can be written as

$$E_R = m_{air} \int_{T_o}^{T_{max}} (A + bT)\, dT \tag{2}$$

where T_o is the starting temperature in the chamber and T_{max} is the temperature at the peak quasistatic overpressure. The term m_{air} is the mass of air in the test chamber; the explosive mass also produces gas in the chamber, but its contribution is assumed to be negligible for these small charges. Small deviations in the atmospheric pressure or air density also have a negligible effect on the calculation, so it is assumed that air is an ideal gas whose density ρ_{air} is a constant 1.2041 kg/m^3. Integrating the specific heat expression given above yields

$$E_R = V\Delta P\left[\alpha + \frac{\Delta P}{\beta}\right] \tag{3}$$

where

$$\beta = \frac{2R_m^2\rho_{air}}{b} = 1.1 \text{ MPa}$$

$$\alpha = \frac{A}{R_m} + \frac{2P_o}{\beta} = 2.55.$$

Here ΔP is the peak quasistatic overpressure generated within the chamber, R_m is the specific gas constant for dry air (287.058 J/kg K), and P_o is the ambient pressure. The combustion energy release from the charge can also be written as $E_R = \eta C \Delta H_c^{HE}$ where C is the explosive charge mass, η is an efficiency factor for its reaction (equal to 1 for full reaction), and ΔH_c^{HE} is its enthalpy of combustion. For a

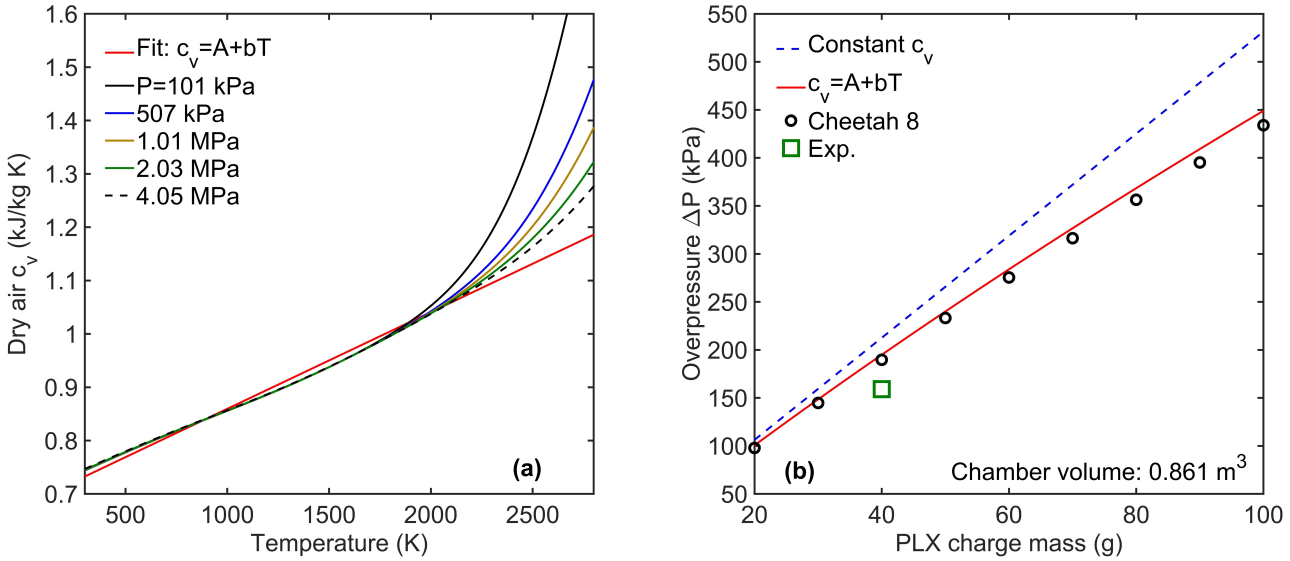

Figure 4. (a) Heat capacity of air at several constant pressures. The linear form is a reasonable fit up to an average chamber temperature of 2000 K. **(b)** Overpressure in the chamber for a bare PLX charge with different heat capacity models. The experimental overpressure falls below the theoretical maximum value, likely due to incomplete carbon afterburn.

known charge mass, efficiency, and chamber volume, solving for the quasistatic overpressure then yields

$$\Delta P = \frac{\beta}{2}\left(\frac{\sigma}{V} - \alpha\right) \tag{4}$$

where

$$\sigma = \left[(\alpha V)^2 + \frac{4V\eta C\Delta H_c^{HE}}{\beta}\right]^{\frac{1}{2}}.$$

The heat of combustion ΔH_c^{HE} for PLX, calculated using Cheetah 8 thermochemical software, is 11.44 MJ/kg. PLX is an under oxidized explosive, with an oxygen balance of −48% assuming CO_2 is formed. Figure 4b shows a comparison of the theoretical maximum overpressure in the chamber for a range of PLX charge sizes; a linear specific heat dependence gives results close to a full Cheetah thermoequilibrium calculation until the quantity of explosive in the chamber is large. The Cheetah calculations account for the air in the chamber as well as the gas generated by the PLX charge. Also shown in Figure 4b is the expression for a constant specific heat,

$$\Delta P = \frac{\eta C\Delta H_c^{HE}}{V}(\gamma - 1) \tag{5}$$

where the adiabatic γ is 1.4 for air and 1.67 for argon. This expression is used in previous work [24], but is less reliable at larger explosive mass to chamber volume ratios. Using the overpressure data shown in Figure 3 and Eq. (3) above, the energy releases for PLX in the experimental chamber are calculated and presented in Table 2. The PLX charge does not completely react in air, likely an artifact of the charge's small size and an incomplete carbon afterburn.

Table 2. Calculated energy release data for explosive tests in air.

	Charge Mass (g)	Peak Overpressure ΔP (kPa)	Total Energy Release E_R (MJ)	Energy Release per gram (MJ/kg)	Energy Release per vol (kJ/cm^3)	Average Efficiency (%)
H15 M/C = 2	39.98	487.4 +/− 2.6	0.88 +/− 0.01	10.76 +/− 0.09	28.37 +/− 0.26	34.2 +/− 3.6
	40.74	499.5 +/− 4.1	0.91 +/− 0.01	11.63 +/− 0.15	28.29 +/− 0.37	
	40.57	445.1 +/− 3.9	0.76 +/− 0.01	9.4 +/− 0.14	24.52 +/− 0.35	
H15 M/C = 3	40.70	535.1 +/− 2.8	1.02 +/− 0.01	7.79 +/− 0.06	19.09 +/− 0.15	24.1 +/− 1.6
	40.60	509.2 +/− 3.1	0.94 +/− 0.01	7.11 +/− 0.07	18.23 +/− 0.17	
6061-Al	40.77	319.4 +/− 3.3	0.41 +/− 0.01	4.8 +/− 0.1	13.14 +/− 0.29	15.5 +/− 0.02
PLX	39.99	159.1 +/− 1.6	0.36 +/− 0.01	8.91 +/− 0.1	10.26 +/− 0.11	76.7 +/− 1.8
	40.01	154.3 +/− 2	0.35 +/− 0.01	8.62 +/− 0.12	9.98 +/− 0.14	

The square in Figure 4b shows that the experimental pressure of the 40 g PLX charge is below the theoretical maximum energy release, corresponding to an efficiency $\eta =$ 76.7 %. This sets the baseline for other shots with additional metal combustion from the reactive material case. The PLX shots in argon have even lower efficiency, as expected. Equation (5) with an adiabatic γ of 1.67 gives an efficiency of roughly 27.5 % for the PLX in the inert atmosphere compared to its heat of combustion in air.

3.2 Reactive Material Cased Charges

The energy release from PLX charges with reactive material cases is now compared to the bare explosive shots. Example cases are shown in Figure 1a; these were filled with PLX and detonated in air. Cases made from aluminum 6061-T6 alloy with an M/C ratio of 2 were also tested as a baseline comparison. The video was captured with a Phantom v2512 high-speed camera and several frames from a representative test with an H15 RM case in the air are presented in Figure 5. The metal combustion primarily occurs upon the impact of the fragment cloud with the chamber walls. There is a distinct period with little light emission after the PLX detonation and before this wall impact. The impact begins after approximately 450 microseconds, and the combustion continues vigorously for several tens of milliseconds. This behavior, seen in other enclosed detonation tests of reactive material cases [12], shows that secondary impact and fragmentation on the chamber walls are important at this scale. The relative importance of wall impact is expected to vary with the chamber volume and geometry, however. At much larger volumes, small particles may decelerate behind the air blast and never impact the wall. Other chamber geometries would affect air blast reflections which might alter mixing and combustion. The results in this work can serve as validation for fragmentation and combustion models of reactive material cases, but as with most non-ideal explosives caution should be used when extrapolating to other scales.

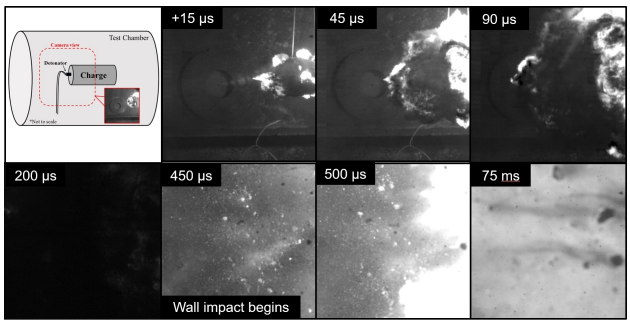

Figure 5. High-speed video frames of an experiment conducted in air atmosphere.

The overpressure for the M/C = 2 and M/C = 3 cases are presented in Figures 6a and 6b respectively. The overpressure for the bare PLX high explosive in the air is also shown for reference. Peak overpressure is reached at a later time in the cased shots than for a bare explosive charge, consistent with later combustion occurring on impact with the chamber walls.

The interpretation of the overpressure is slightly more complex for cased explosive shots than for the caseless PLX. It is again assumed that the combustion energy is only transferred into the gases present in the chamber. The energy released by the reactive material case is then

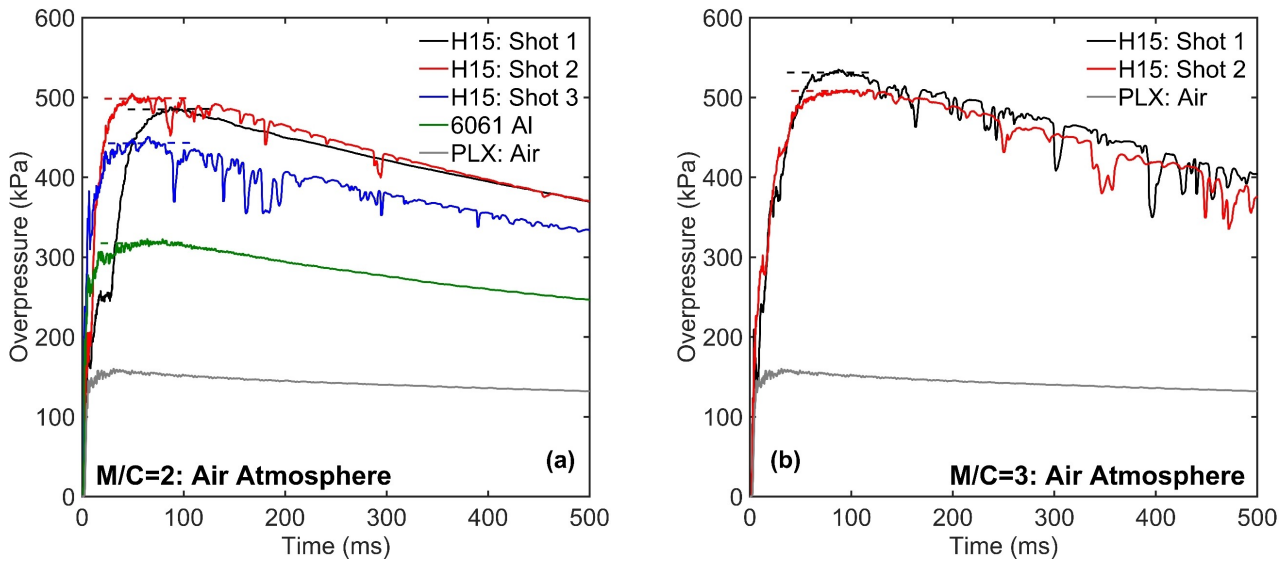

Figure 6. Overpressure vs. time curves for reactive material cased charges detonated in the air. Horizontal dashed lines indicate the maximum quasistatic overpressure used in Equation 6.

$$E_R^{RM} = V\Delta P\left[\alpha + \frac{\Delta P}{\beta}\right] - \eta C \Delta H_c^{HE} \quad (6)$$

where ΔH_c^{HE} is again the heat of combustion of the explosive charge, and η is the percent efficiency of the isolated HE in the experimental chamber (76.7% for these PLX charges). This expression assumes that the kinetic energy of the case is ultimately converted back into internal energy when the fragments impact the chamber walls or decelerate in air. Some of this kinetic energy will be lost in impact on the walls, and some will be retained as internal energy in the solid debris. These are assumed to be small effects, allowing a bare high explosive charge to serve as the baseline comparison for the energy release. The above expression also assumes the solid debris does not contribute to the heat capacity.

The peak quasistatic overpressure ΔP occurs at 60–100 ms in these tests, and is noted with dashed horizontal lines in Figures 6a and 6b. This pressure is distinct from early time blast transients in the chamber, which are smoothed out by the processing of the overpressure discussed above. These transients can have a higher pressure than the quasistatic value but primarily arise from the initial detonation and not from the slow afterburn and post-detonation combustion.

Figure 7 and Table 2 present the energy release of the H15 cases calculated using Equation 6. Note that all information for the cased shots is reported with the contribution of the PLX charge removed (by the final term in Equation 6). As expected, the thicker M/C = 3 cases have a higher total energy release compared to the M/C = 2 cases due to their larger mass. However, on a per mass or per volume basis, there is a decrease in combustion efficiency with the thicker case. A natural explanation for this would be the reduction in blowoff velocity at the larger mass to charge ratio. This would result in a lower wall impact velocity, less RM ignition on impact, and thus a reduced combustion efficiency compared to the lower M/C. However, the fragmentation results presented below suggest the situation may be more complex for this particular aluminum material. Despite having a presumably smaller impact velocity on the chamber walls, the M/C = 3 case produces similar or slightly more fine fragments per unit mass than the thinner one. This is discussed further in the fragmentation results.

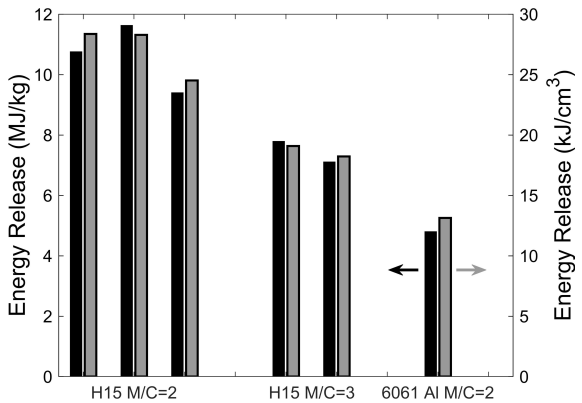

Figure 7. Calculated values of the energy release of aluminum cases. The RM cases vary slightly in density.

The heat of combustion of aluminum is 31.1 MJ/kg; as shown in Figure 7, all cases release less than this theoretical maximum. On a per mass basis, the M/C = 2 aluminum RM cases are roughly 34% efficient, the M/C = 3 cases are 24% efficient, and the aluminum 6061 sample (which is not made from pressed powder) is 16% efficient. For many applications, however, the energy release on a per-volume basis may be of more concern, as in a volume-constrained warhead. In this regard, the energy release of even these simple RM cases provides two to three times more energy density than the liquid explosive. These values are also shown in Figure 7.

The standard assumption in these tests is that the combustion process is completed before the peak quasistatic overpressure is reached. This is considered by examining the light emission in the high-speed video of the chamber. Figure 8 plots the normalized light emission as well as the chamber overpressure for a representative RM cased shot. This light emission was calculated by taking the average intensity of every pixel in the camera view for each frame and normalizing it to the maximum value.

A value of one represents pixels consistent with the peak light emission observed during the event. Most pixels are saturated in the first 25 ms. After this, a drop in light emission begins at approximately 70 ms and then the peak quasistatic overpressure starts to decay around 100 milliseconds. The drop in emission thus begins at least 30 ms before the peak quasistatic overpressure; it may begin even

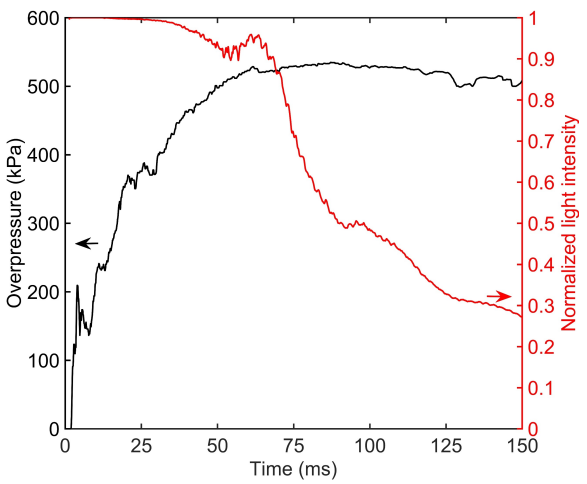

Figure 8. Comparison of overpressure and normalized light emission from an RM test. Representative data from the H15, M/C = 2 test.

earlier but is masked by the saturation. This result provides some degree of validation that the peak quasistatic overpressure in the chamber does indeed approximate the end of reaction as is commonly assumed.

3.3 Fragmentation

The size distribution of recovered fragments is now compared with the overpressure generated during the combustion event. Two separate experiments were performed to collect fragmentation data, shown schematically in Figure 9.

The primary fragmentation event when the case is blown outward by the expanding detonation products is examined by surrounding the charge assembly with a snow soft-catch layer to gently decelerate the fragments before wall impact. Ref. [16] gives additional details on the production and processing of the snow. The charge was promptly detonated to avoid as much degradation of the snow medium as possible. Following the detonation, the snow was carefully removed from the chamber and warm ethanol was added to help separate the metal fragments. The resulting solution was allowed to settle and then decanted several times to remove as much liquid as possible. It was subsequently dried under a vacuum to prepare the fragments for analysis. Collected fragments were carefully sieved through a traditional sieve stack to analyze the fragment distributions.

The secondary fragmentation, in which primary fragments strike the chamber walls, was studied by filling the chamber with argon. The use of an inert atmosphere allows fragment impact on the walls to occur while preventing aerobic combustion of the aluminum. In principle, some species in the detonation products could react with the metal; however, the PLX charge is already under oxidized and the amount of product gas is small compared to the chamber volume. No visible combustion is observed after secondary impact in the argon-filled tank, as demonstrated in Figure 10. Secondary fragments were recovered by thoroughly sweeping out the experimental chamber.

Figure 11 presents a photograph of all fragments from a representative snow recovery test, highlighting the large quantity of fine debris recovered. At least 20% of the original case mass ends up in fragments smaller than 45 μm, and no fragments are larger than 1.2 mm.

Figure 12a presents the cumulative distribution function (CDF) data for M/C = 2 and M/C = 3 H15 cases detonated in the soft-catch environment, along with the aluminum 6061-T6 alloy case as a baseline comparison. The data is presented as fragment cumulative mass percentage versus linear fragment size. The raw data for these fragment distributions is given in Tables S1 and S2.

Primary fragmentation of the brittle RM materials results in dramatically finer fragments than the ductile bulk 6061 alloys, as expected. However Figure 12a shows that, counterintuitively, the thicker M/C = 3 reactive material cases result in slightly more fragments below 400 μm per unit mass compared to the M/C = 2 cases. This result is discussed further below. Figure 12b shows the recovered secondary fragments for which cases were detonated in an argon-filled chamber. Here again, two of the thicker RM cases produce more fine fragments when normalized by mass.

For the M/C = 2 cases, the combustion efficiency is approximately 34%. A similar percentage of the second fragment mass is below 100 μm for this case thickness. However, a similar correspondence is not seen for the M/C = 3 cases. The thicker case produces more fine fragments as a percentage of the total case mass but displays a lower combustion efficiency (Figure 7) compared to the thinner case.

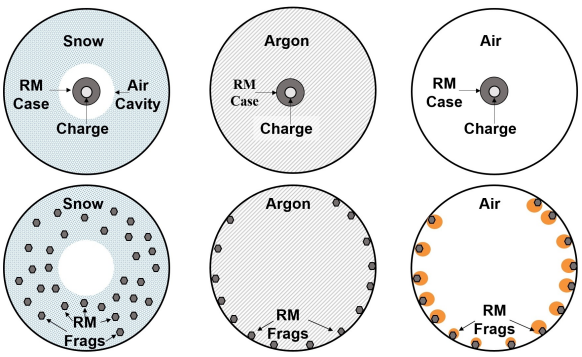

Figure 9. Test configurations for snow (primary fragment recovery), inert argon (secondary fragment recovery), and air atmosphere (overpressure) experiments.

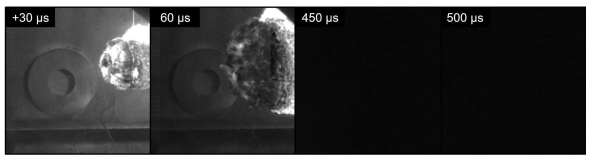

Figure 10. Frames from the inert atmosphere test. Note lack of visible combustion on chamber walls in the final two frames.

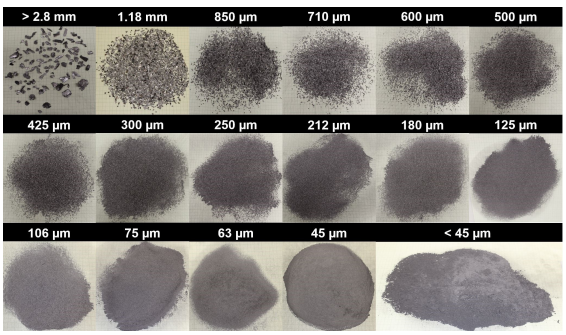

Figure 11. Photographs of primary fragments recovered in each sieve from a typical RM case test.

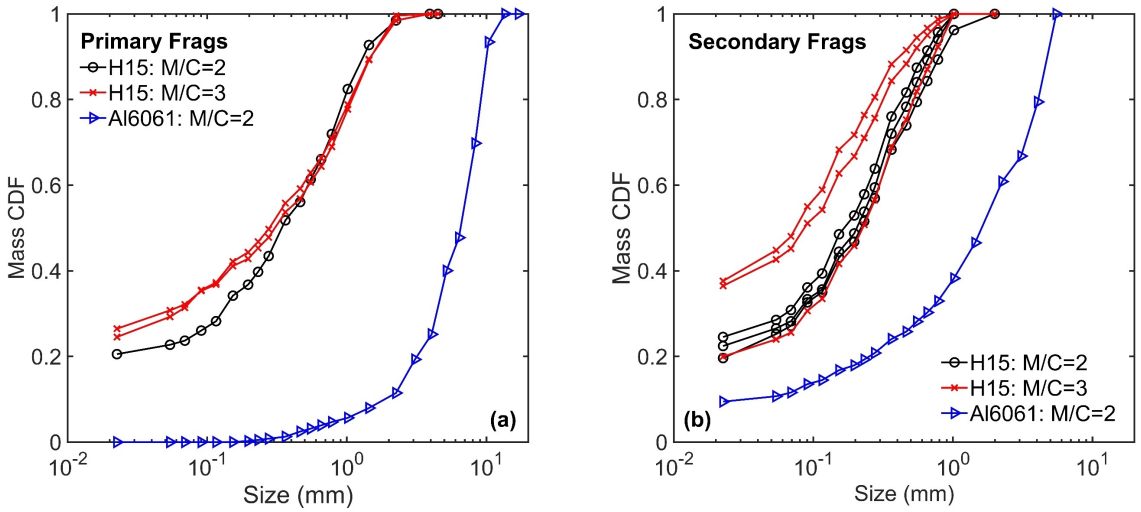

Figure 12. Fragment distributions from **(a)** snow recovery-primary fragments **(b)** argon atmosphere-secondary fragments.

The lower combustion efficiency may be related to the reduced case blowoff velocity as discussed above, but lower blowoff velocity would normally result in fewer fine fragments. This suggests that it may not be purely the degree of fragmentation or the overall surface area of fragments limiting the extent of combustion; there may also be effects such as limited oxidizer mixing with the secondary fragments on a boundary layer near the walls.

Another potential explanation for this observation is the formation of a shock-compacted region generated by the HE charge. The atomized aluminum used to fabricate these cases is completely unalloyed and is extremely ductile. The Hopkinson bar data in Figure 2 and prior work on a similar aluminum compact show that in uniaxial compression the material can sustain enormous plastic strain [16]. The region in direct contact with the explosive will receive a large induced shock from the passing detonation, which may compact the inner portion of the case and result in dynamically altered mechanical properties that would not be seen in Hopkinson bar and Brazilian testing. Given that the same HE charge was used in all tests, the thicker case would provide more material outside that shock-compacted zone compared to the thinner case. The greater excess of material outside of the shock-compacted zone could lead to an increase in fine fragments compared to the thinner cases as is observed.

Alternatively, the thicker cases may provide a greater volume for defects as nucleation sites for cracks in the radial direction during the fragmentation process. However, in preliminary tests on other compacted metal powder cases we have not observed the same behavior seen here; thicker cases tend to produce fewer finer fragments per unit mass than thinner cases with a constant burster charge, consistent with expectations. Thus the trend here may be an artifact of the highly ductile nature of the pure, atomized aluminum or the natural variability in the isostatically pressed cases with non-negligible porosity. Additional tests on other reactive materials are desirable to clarify this point.

The fragment collection process does not appear to result in unwanted oxidation or reaction that may alter the size distributions. Figure 13 shows the X-ray diffraction spectra comparing the starting raw H15 powder to the finest fragments (< 45 μm) recovered from the snow catch, inert atmosphere, and air atmosphere tests. These spectra indicate no observable oxide products even in the finest fragments in snow or inert atmosphere tests.

Scanning electron micrographs documenting the starting powder pressed sample and recovered fragment morphology are presented in Figures 14a–f. Figure 14a presents

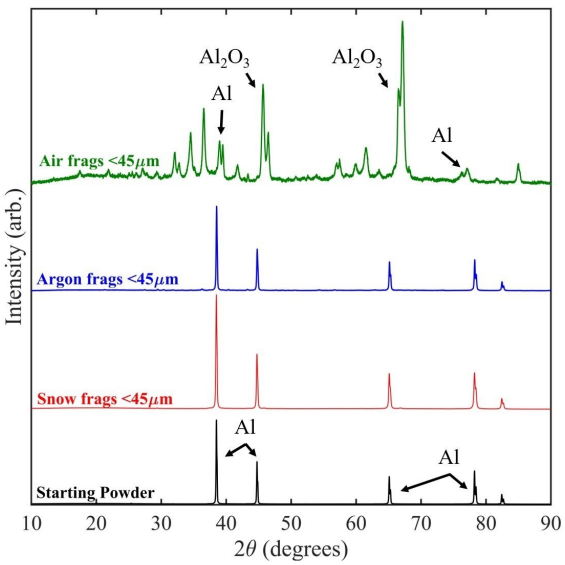

Figure 13. XRD spectra of starting H15 powder and samples of the finest fragments recovered from explosive tests.

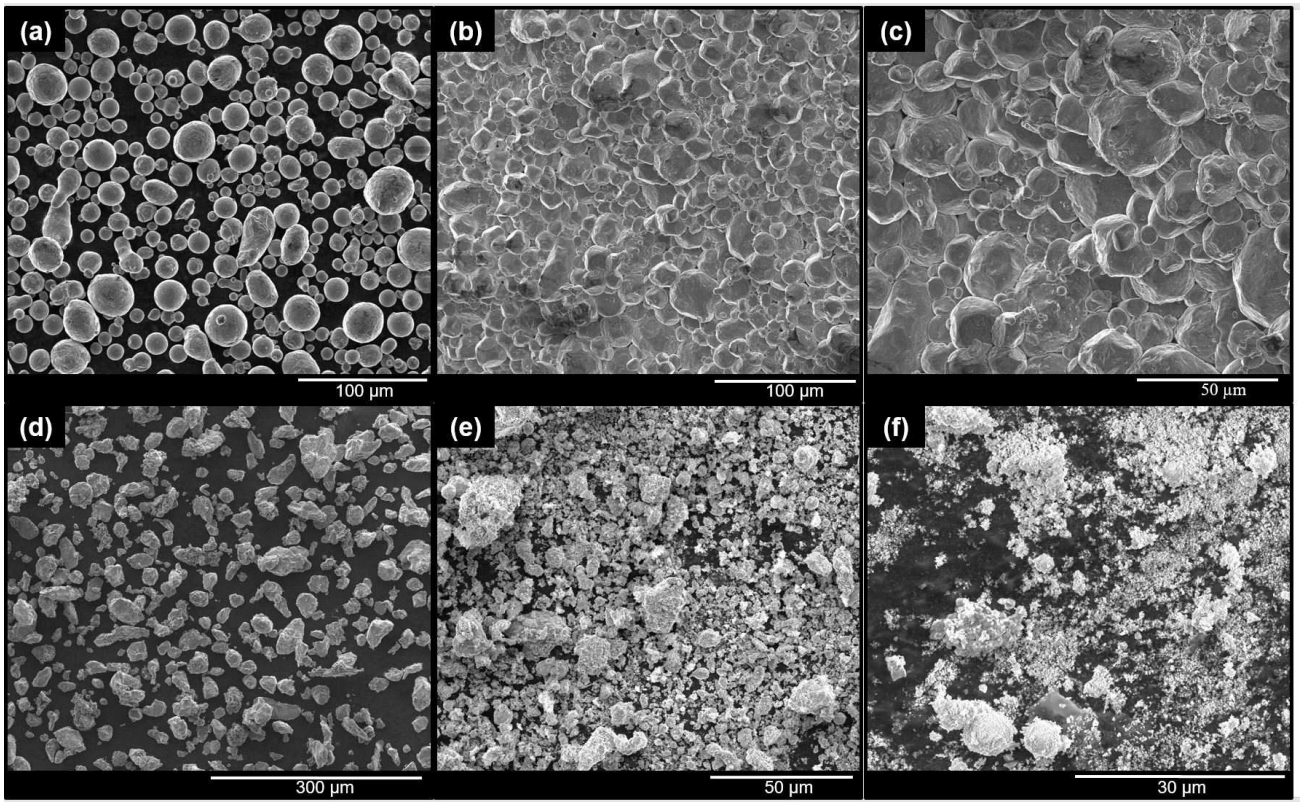

Figure 14. Scanning electron micrographs of H15 aluminum **(a)** starting powder, **(b)** fracture surface pressed sample, **(c)** fracture surface of a pressed sample, **(d)** primary fragments from snow recovery shot, **(e)** secondary fragments from inert atmosphere test, and **(f)** fine fragments and oxide combustion products from the air atmosphere shot.

the raw feedstock, which is typical of an atomized metal powder. Figures 14b and 14c present micrographs of representative pressed sample surfaces. As has been noted in previous work [16, 23], failure of these brittle metal compacts occurs along original particle boundaries, with minimal intraparticle cleavage or failure. Figure 14d presents a sample of the finest fragments (below 45 µm) recovered from the snow catch experiments; these show no evidence of oxidation or surface morphology changes. Figure 14e shows fragments recovered from the inert tests. Unlike the shots in a snow cavity, the fragments are not protected from the fireball. They do show some surface alterations and carbon residue from the explosive, but these are not significant enough to appear in X-ray diffraction. Figure 14f shows fine debris from the tests in the air atmosphere, which is comprised predominately of aerosols generated by the combustion process.

4 Conclusion

This work presents the fragmentation of a brittle reactive material case along with its energy release following detonation in a closed chamber. A basic aluminum reactive material made from the cold isostatically-compacted atomized powder was compared to a standard aluminum 6061-T6 alloy and bare explosive. The extent of combustion is inferred from the quasistatic overpressure generated in the chamber. The reactive material cases produce two to three times the total combustion energy per volume as compared to the baseline alloy or the bare explosive. This is true even though only approximately one-third of the reactive material case combusts according to overpressure measurements. The metal reaction begins primarily on impact with the walls rather than during explosive launch or supersonic flight in the air. The thicker tested case had a lower energy release per unit mass, despite producing similar or even slightly higher percentages of fine pyrophoric fragments below 100 µm. The combustion for this particular reactive material may thus depend not only upon the amount of fine debris or total surface area of the fragment cloud but also upon proper mixing with oxidizer or shock compaction during explosive launch.

Acknowledgements

The authors gratefully acknowledge support from the Office of Naval Research grant N0001420WX00021 (program managers Chad

Stoltz and Matt Beyard) and Defense Threat Reduction Agency grant HDTRA1034195 (program manager Jeff Davis).

Data Availability Statement

The data that supports the findings of this study are available in the supplementary material of this article and on request from the author.

References

[1] D. L. Frost, S. Goroshin, J. Levine, R. Ripley, F. Zhang, Critical conditions for ignition of aluminum particles in cylindrical explosive charges, *Shock Compression of Condensed Matter*, July 31–August 5, **2005**, Baltimore, MD. DOI: 10.1063/1.2263484.
[2] Y. Aly, M. Schoenitz, E. L. Dreizin, Aluminum-metal reactive composites, *Combust. Sci. Technol.* **2011**, *183*, 1107–1132. DOI: 10.1080/00102202.2011.584090.
[3] E. L. Dreizin, M. Schoenitz, Correlating ignition mechanisms of aluminum based reactive materials with thermoanalytical measurements, *Prog. Energy Combust. Sci.* **2015**, *50*, 81–105. DOI: 10.1016/j.pecs.2015.06.001.
[4] D. Stamatis, X. Jiang, E. Beloni, E. Dreizin, Aluminum burn rate modifiers based on reactive nanocomposite powders, *Propellants Explos. Pyrotech.* **2010**, *35*, 260–267. DOI: 10.1002/prep.200900009.
[5] N. G. Yen, L. Y. Wang, Reactive metals in explosives, *Propellants Explos. Pyrotech.* **2012**, *37I*, 143–155.
[6] L. Maiz, W. A. Trzcinski, Detonation characteristics of new aluminized enhanced blast composites, *Propellants Explos. Pyrotech.* **2018**, *43*, 650–656. DOI: 10.1002/prep.201800094.
[7] K. Kappagantula, M. Pantoya, E. Hunt, Impact ignition of aluminum-teflon based energetic materials impregnated with nanostructured carbon additives, *J. Appl. Phys.* **2012**, *112*, doiL10.1063/1.4737118.
[8] M. Raftenburg, W. Mock Jr., G. C. Kirby, Modeling the impact deformation of rods of a pressed PTFE/Al composite mixture, *Int. J. Impact Eng.* **2008**, *35*, 1735–1744. DOI: 10.1063/1.3480020.
[9] M. Losada, S. Chaudhuri, Finite size effects on aluminum/Teflon reaction channels under combustive environment: A Rice-Ramsperger-Kassel-Marcus and transition state theory study of fluorination, *J. Chem. Phys.* **2010**, *133*, 134305.
[10] T. Sippel, S. Son, L. Groven, Altering reactivity of aluminum with selective inclusion of polytetrafluorethylene through mechanical activation, *Propellants Explos. Pyrotech.* **2013**, *38*, 286–295. DOI: 10.1002/prep.201200102.
[11] P. Chiu, K. Olney, D. Benson, C. Braithwaite, A. Collins, V. Nesterenko, Dynamic fragmentation of Al–W granular rings with different mesostructures, *J. Appl. Phys.* **2017**, *121*, 045901. DOI: 10.1063/1.4973730.
[12] F. Zhang, M. Gauthier, C. Cojocaru, Dynamic fragmentation and blast from a reactive material solid, *Propellants Explos. Pyrotech.* **2017**, *42*, 1072–1078.
[13] W. Wilson, F. Zhang, K. Kim, Fine fragmentation distribution from structural reactive material casings under explosive loading, *19th Biennial Conference on Shock Compression of Condensed Matter*, June 14–19 **2015**, Tampa, Florida. DOI: 10.1063/1.4971531.
[14] Y. Huang, G. A. Risha, V. Yang, R. A. Yetter, Effect of particle size on combustion of aluminum dust in air, *Combust. Flame* **2009**, *156*, 5–13. DOI: 10.1016/j.combustflame.2008.07.018.
[15] M. Trunov, M. Schoenitz, E. L. Dreizin, Ignition of Aluminum Powders Under Different Experimental Conditions, *Propellants Explos. Pyrotech.* **2005**, *30*, 36–43. DOI:10.1002/prep.200400083.
[16] J. Kline, J. P. Hooper, The effect of annealing on the impact fragmentation of a pure aluminum reactive material, *J. Appl. Phys.* **2019**, *125*, DOI:10.1063/1.5094444.
[17] J. Hooper, Impact fragmentation of aluminum reactive materials, *J. Appl. Phys.* **2012**, *112*, DOI:10.1063/1.4746788.
[18] J. J. Chen, B. Q. Guo, H. B. Liu, P. W. Chen, Dynamic Brazilian test of brittle materials using the Split Hopkinson Bar Pressure-bar and digital image correlation, *Strain* **2014**, *50*, 563–570. DOI: 10.1111/str.12118.
[19] C. Johnstone, C. Ruiz, Dynamic testing of ceramics under tensile stresses, *Int. J. Solids Struct.* **1995**, *32*, 2647–2656. DOI:10.1016/0020-7683(94)00287-.
[20] Suggested methods for determining the tensile strength of rock materials, *Int. J. Rock Mech. Min. Sci. & Geomech. Abs* **1978**, *15*, 99–103. https://doi.org/10.1016/0148-9062(78)90003-7.
[21] M. Tang, J. P. Hooper, Impact fragmentation of a brittle metal compact, *J. Appl. Phys.* **2018**, *123*, 175901. DOI: 10.1063/1.5026711.
[22] S. Wang, J. Kline, B. Miles, J. Hooper, Reactive fragment materials made from an aluminum-silicon eutectic powder, *J. Appl. Phys.* **2020**, *128*, 065903.
[23] M. W. Chase, NIST-JANAF Thermochemical Tables, *American Institute of Physics*, Washington DC, **1998**.
[24] R. Ames, Energy release characteristics of impact initiated energetic materials, *MRS Proceedings* **2005**, *896*, 0896-H03–08.

Manuscript received: January 14, 2021
Revised manuscript received: March 22, 2021
Version of record online: ■■, ■■■

FULL PAPER

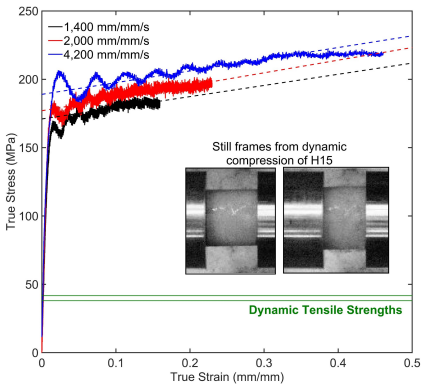

*J. C. Kline, B. P. Mason, J. P. Hooper**